Photon regions, shadow observables, and constraints from M87* of a charged rotating black hole

Yuan Meng and Xiao-Mei Kuang*

Center for Gravitation and Cosmology, College of Physical Science and Technology, Yangzhou University, Yangzhou 225009, China

Zi-Yu Tang

School of Fundamental Physics and Mathematical Sciences, Hangzhou Institute for Advanced Study, UCAS, Hangzhou 310024, China and School of Physical Sciences, University of Chinese Academy of Sciences, Beijing 100049, China

(Received 12 April 2022; accepted 12 August 2022; published 2 September 2022)

Inspired by the observations of the supermassive black hole M87* by the Event Horizon Telescope (EHT), a remarkable surge in black hole physics is to use the black hole shadow's observables to distinguish between general relativity and modified theories of gravity, which could also help to reveal the astrophysical nature of the central black hole in the EHT observation. In this paper, we study a charged rotating black hole in conformal gravity, in which the term related to the charge has different falloffs from the usual Kerr-Newman (KN) black hole. We investigate the spacetime properties including the horizons, ergospheres, and photon regions; then, we show the boundary of the black hole shadow and investigate its characteristic observables. These features closely depend on the spin and charge parameters, which are compared with those in Kerr and KN black holes. Then, presupposing that M87* is a charged rotating black hole in conformal gravity, we constrain the black hole parameters via the observational constraints from EHT. We find that the constraints on the inferred circularity deviation ($\Delta C \lesssim 0.1$) and shadow axial ratio ($1 < D_x \lesssim 4/3$) for M87* are satisfied for the entire parameter space of the charged rotating black hole in conformal gravity. However, the shadow angular diameter $\theta_d = 42 \pm 3$ μas gives an upper bound on the parameter space. Our findings indicate that the current charged rotating black hole in conformal gravity could be a candidate for astrophysical black holes. Moreover, the EHT observation of the axial ratio D_x may help us to distinguish between a Kerr black hole and the current charged rotating black hole in conformal gravity in some parameter space.

DOI: 10.1103/PhysRevD.106.064006

I. INTRODUCTION

Since Bardeen addressed that the shadow of a Kerr black hole would be distorted by its spin [1], in contrast to the perfect circular shadow of a Schwarzschild black hole [2], the study of the shadow of a rotating black hole has blossomed with the motivation that the trajectories of light near a black hole and its shadow are closely connected with the essential properties of the background theory of gravity. Thus, physicists can use a black hole's shadow to reveal its near-horizon features via analytical investigations or numerical simulation (see Refs. [3–31] and references therein). Moreover, the size and distortion of a shadow [32,33], which can be calculated via its boundary, has been widely investigated to estimate a black hole's parameters in both general relativity (GR) and modified theories of gravity (MG), with or without additional sources surrounding the black hole [34–53]. This can be seen as one way that black hole shadows could distinguish GR and other theories of gravity, or as a way to acquire information on the surrounding matter, though it was found that these theoretical features of shadows are usually not sufficient to distinguish black holes in different theories or confirm the details of the surrounding matter. More details about black hole shadows can be found in Refs. [54,55].

More recently, the Event Horizon Telescope (EHT) Collaboration captured the first image of the supermassive black hole M87*, making black hole shadows a physical reality [56–58]. The shadow of M87* from the EHT observation has a deviation from circularity $\Delta C \lesssim 0.1$, an axis ratio $1 < D_x \lesssim 4/3$, and an angular diameter $\theta_d = 42 \pm 3$ μas. These observations are consistent with the image of a Kerr black hole predicted from GR, but they cannot rule out Kerr or non-Kerr black holes in MG. Thus, the EHT observations of M87*'s shadow could be used to test black holes in the strong gravitational field regime, as

*xmeikuang@yzu.edu.cn

the observational data could constrain the black hole parameters in MG and even distinguish different theories of gravity [47–53,59–61].

In this work, we mainly study the aspects of shadows for a charged rotating black hole in conformal gravity characterized by the spin and charge parameters, in which the charge-related term has different falloffs from the usual Kerr-Newman (KN) black hole. We show more details about this black hole geometry in the next section. The charged rotating black hole we consider here was introduced in Ref. [63] as a solution in conformal gravity, with the Lagrangian

$$L = \frac{1}{2}\gamma C^{\mu\nu\rho\sigma}C_{\mu\nu\rho\sigma} + \frac{1}{3}\gamma F^2, \tag{1}$$

which includes the Weyl-squared term minimally coupled to the Maxwell field. Here $C_{\mu\nu\rho\sigma}$ is the Weyl tensor and $F = dA$ is the strength of the Maxwell field. Conformal gravity was introduced by Weyl as an extension of GR [64] and later studied by 't Hooft and many others in Refs. [65–68]. The analysis of the ghost instability and unitarity of conformal gravity was studied in Refs. [69,70]. Different from GR, in conformal gravity dark matter or dark energy is not necessary to solve several cosmological and astrophysical problems, and readers can refer to Ref. [71] for more details on this comparison. In addition, Maldacena addressed that conformal gravity would reduce to Einstein gravity for a certain boundary condition and there could be a holographic connection between the two theories of gravity [72]. Such advantageous features indicate that the contents of conformal gravity deserve to be explored further. One natural direction is black hole shadows, as the recent progress of the EHT opens a new window to test the strong-field regime.

The shadow boundary of a Kerr-like metric in conformal gravity was investigated in Ref. [73]. Here, we consider the charged rotating black hole geometry and extensively study the aspects of its shadow. Starting from the null geodesics, we study the photon regions and then figure out the shadow boundary of the black hole. We also analyze the characteristic observables, i.e., the shape, size, and distortion of the shadows, and estimate the black hole parameters from given observables. Then, we consider M87* as a charged rotating black hole in conformal gravity and constrain its black hole parameters using the EHT observations.

The remainder of this paper is organized as follows. In Sec. II we study the horizons, static limit, and other spacetime properties of a charged rotating black hole in conformal gravity. In Sec. III we obtain the photon region by analyzing the null geodesics. In Sec. IV, with the use of Cartesian coordinates, we show the shadow boundary with various values of the parameters for observers at a finite distance. In Sec. V we investigate the size and deformation of the black hole shadow for an infinitely distant observer and address the parameter estimation using the shadow's observables, from which we also calculate the energy emission rate. In Sec. VI, by presupposing that M87* is a charged rotating black hole in conformal gravity, we constrain the black hole parameters using the EHT observations. The last section presents our closing remarks.

II. CHARGED ROTATING BLACK HOLE IN CONFORMAL GRAVITY

Starting from Eq. (1), a rotating charged black hole in conformal gravity was constructed in Ref. [63] with the metric

$$\begin{aligned} ds^2 = {} & \Sigma\left(\frac{1}{\Delta_r}dr^2 + d\vartheta^2\right) + \frac{1}{\Sigma}((\Sigma + a\chi)^2\sin^2\vartheta - \Delta_r\chi^2)d\varphi^2 \\ & + \frac{2}{\Sigma}(\Delta_r\chi - a(\Sigma + a\chi)\sin^2\vartheta)dtd\varphi \\ & - \frac{1}{\Sigma}(\Delta_r - a^2\sin^2\vartheta)dt^2, \end{aligned} \tag{2}$$

where

$$\begin{aligned} \Sigma &= r^2 + a^2\cos^2\vartheta, \qquad \chi = a\sin^2\vartheta, \\ \Delta_r &= r^2 - 2mr + a^2 + \frac{\beta r^3}{6m}. \end{aligned} \tag{3}$$

Here, m, $\beta = p^2 + q^2$, and a are the mass, charge, and rotation parameters, respectively. When the charge parameter vanishes, the metric reduces to the well-known Kerr black hole. This black hole is different from the usual KN black hole where the charge term in Δ_r is simply a constant β, instead of the cubed term $\beta r^3/6m$ in conformal gravity. We note that, compared to the expression for the rotating charged solution in Ref. [63], here we focus on the case where the integral constant Λ is zero.[1]

A. Black hole horizons

It is known that $\Sigma \neq 0$ and $g^{rr} = 0$ can determine a black hole's horizons, which correspond to the positive roots of

$$\Delta_r = r^2 - 2mr + a^2 + \frac{\beta r^3}{6m} = 0. \tag{4}$$

There are three roots to the above equation. Depending on m, a, and β, the three roots can have two real positive values, one real positive value, or no real positive value. The three cases correspond to the metric (2) describing a nonextremal black hole with event horizon (r_+) and Cauchy horizon (r_-), an extremal black hole with event horizon $r_{\rm ex} = r_+ = r_-$, or no black hole sector, respectively. When β is smaller than the critical value from the extremal condition

[1]We thank professor Hai-Shan Liu for reminding us of this point.

$$\beta_{\rm ex} = \frac{4(8m^4 - 9a^2m^2 + \sqrt{m^2(4m^2 - 3a^2)^3})}{9a^4}, \quad (5)$$

the metric describes a nonextremal black hole with $0 < r_- < r_+$. A naked singularity emerges when $\beta > \beta_{\rm ex}$ because in this case none of the three roots have a real positive value. When $\beta = 0$ the horizons $r_\pm$ reduce to $m \pm \sqrt{m^2 - a^2}$, with $|a| \leq m$ (Kerr case). The extremal value $\beta_{\rm ex}$ is different from that for a KN black hole ($\beta_{\rm ex}^{\rm KN} = m^2 - a^2$). However, for $a \to 0$ we have $\beta_{\rm ex} \to +\infty$, which indicates that the black hole is always nonextremal, in contrast to the finite value $\beta_{\rm ex}^{\rm KN} = m^2$ for a Reissner-Nordström black hole. The above scenarios in (a, β) parameter space are shown in Fig. 1, where the case for a KN black hole is also shown for comparison.

Note that here all parameters can be rescaled to be dimensionless, depending on their dimensions related to m; for example, a/m, r/m, and β are dimensionless quantities. Throughout this article these quantities are dimensionless, and for simplicity we set $m = 1$ in the calculations unless stated otherwise.

The explicit dependences of the horizons on the parameters are shown in Fig. 2. It is obvious that as β or a increases, r_+ decreases while r_- increases; as the extremal condition (5) is satisfied, r_+ and r_- converge to $r_{\rm ex}$ which decreases as β increases but increases as a increases (see the solid black curves). Here the effects of the charge and spin parameters on r_+ and r_- are similar to that in KN spacetime where, however, the extremal horizon is $r_{\rm ex}^{\rm KN} = m$ and independent of the charge and spin parameters.

B. Static limit surface

For a rotating black hole, the event horizon of the black hole does not coincide with the static limit surface, at which the asymptotical time-translational Killing vector is null and therefore we have

$$g_{tt} = -\frac{1}{\Sigma}(\Delta_r - a^2 \sin^2\vartheta) = 0. \quad (6)$$

Depending on the values of a, β, and ϑ, there are three possibilities for the roots of the above equation: no real positive root, a double real positive root, and two real positive roots. We denote the real positive roots as r_{SL_-} and r_{SL_+}, with $r_{SL_-} < r_{SL_+}$. The explicit expressions for the solutions are so complicated that we do not show them here; instead, we plot their behaviors in Fig. 3. From the figures we can see that there exists at least one border on which the two static limit surfaces coincide, $r_{SL_-} = r_{SL_+}$, i.e., the extremal case with one real positive root.

Here we will not explicitly describe the dependence of $r_{SL_\pm}$ on the parameters a, β, and ϑ. What we really want to show is that the ergoregion of this rotating black hole is bounded between $r_+ < r < r_{SL+}$ and $r_- < r < r_{SL-}$, in which the timelike killing vector becomes spacelike ($g_{tt} > 0$). In particular, when $\Sigma = 0$, which requires both $r = 0$ and $a\cos\vartheta = 0$, the spacetime has a true physical singularity. Apart from this ring singularity, the sphere $r = 0$ is regular. Besides, for $g_{\varphi\varphi} < 0$, the spacetime violates the causality condition because of the closed timelike curves. More detailed exhibitions of the horizons, ergoregions, singularity, and causality-violating regions will be presented later, together with the photon regions.

III. NULL GEODESICS AND PHOTON REGIONS

The propagation of light near a black hole is significant in both theoretical physics and astrophysics, particularly for circular orbits. For photons, circular orbits outside the event

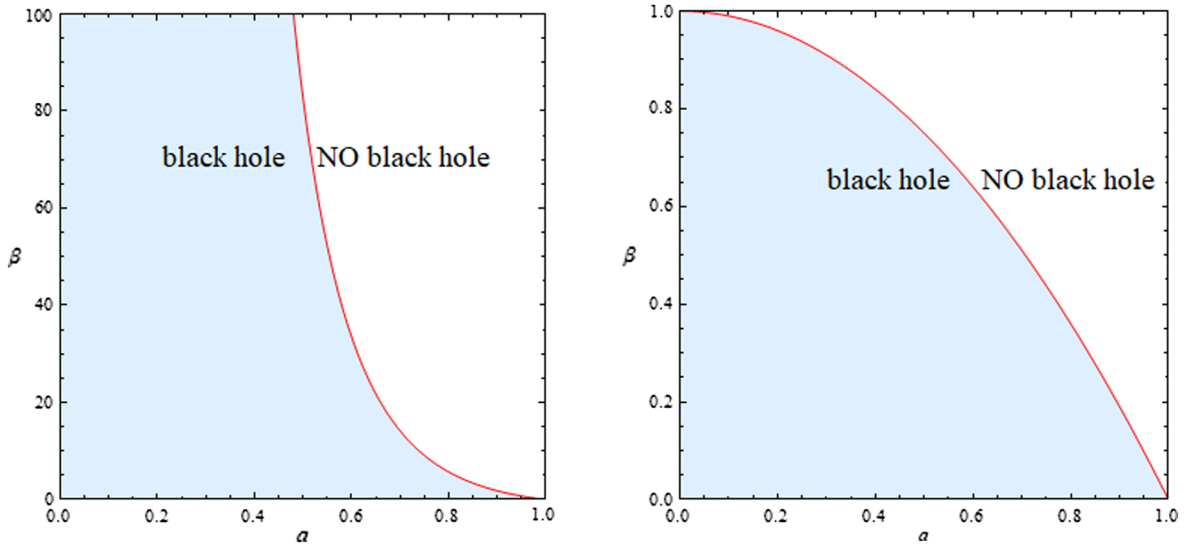

FIG. 1. Parameter space (a, β) of a charged rotating black hole in conformal gravity (left) and a KN black hole (right). The red curves correspond to the extremal cases which separate black holes (blue regions) from naked singularities (white regions).

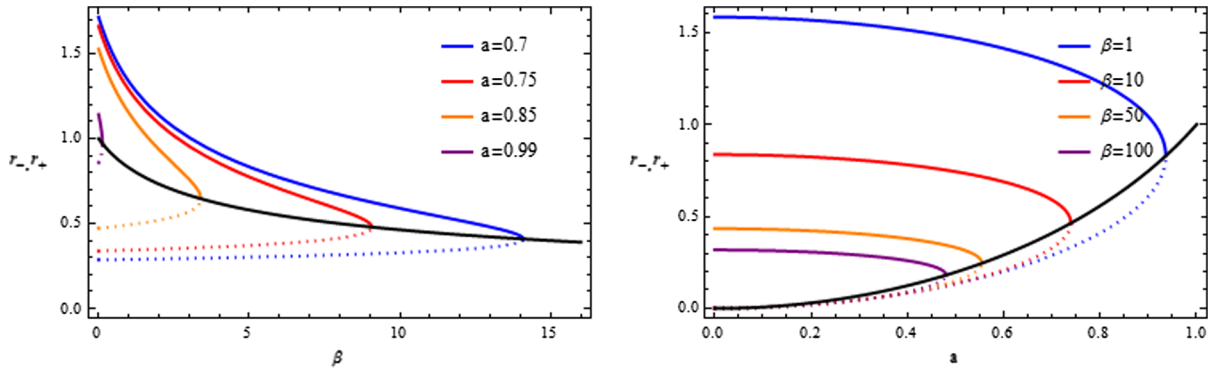

FIG. 2. Event horizon r_+ (solid curve) and Cauchy horizon r_- (dashed curve) with various values of a and β. The solid black curve represents the extremal case where the event horizon and Cauchy horizon coincide.

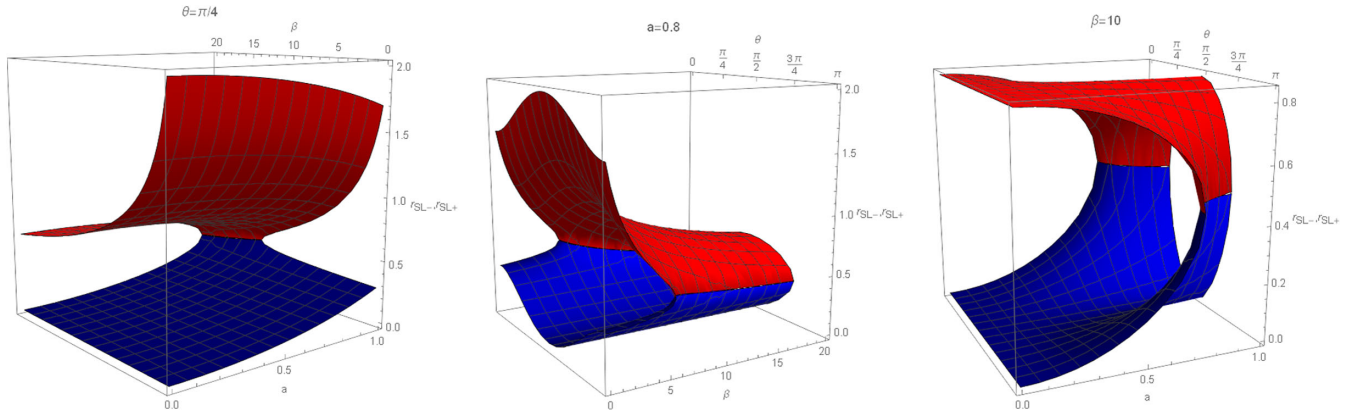

FIG. 3. Static limit surfaces with fixed ϑ, a, and β, respectively, where the red surface denotes r_{SL_+} while the blue surface denotes r_{SL_-}.

horizon of a black hole are usually unstable. This indicates that a slight perturbation can make the photons fall into the black hole or escape to infinity; the latter can constitute a photon ring that confines the black hole image for distant observers. Therefore, we start from the geodesics of the photons in order to analyze the photon regions and the shadow images in the charged rotating black hole spacetime (2) in conformal gravity.

We first consider particles with mass μ, whose Lagrangian of which reads $\mathcal{L}=\frac{1}{2}g_{\mu\nu}\dot{x}^\mu\dot{x}^\nu$. Here a dot represents a derivative with respect to the affine parameter λ, is which related to the proper time via $\tau=\lambda\mu$. Following Ref. [74], we introduce the Hamilton-Jacobi equation

$$\mathcal{H}=-\frac{\partial S}{\partial\lambda}=\frac{1}{2}g_{\mu\nu}\frac{\partial S}{\partial x^\mu}\frac{\partial S}{\partial x^\nu}=-\frac{1}{2}\mu^2, \tag{7}$$

where $\mathcal{H}$ and S are the canonical Hamiltonian and the Jacobi action. With the conserved quantities

$$E:=-\frac{\partial S}{\partial t}=-g_{\varphi t}\dot{\varphi}-g_{tt}\dot{t} \quad \text{and} \quad L_z:=\frac{\partial S}{\partial\varphi}=g_{\varphi\varphi}\dot{\varphi}+g_{\varphi t}\dot{t}, \tag{8}$$

the Jacobi action can be separated as

$$S=\frac{1}{2}\mu^2\lambda-Et+L_z\varphi+S_r(r)+S_\vartheta(\vartheta), \tag{9}$$

where E and L_z are the constants of motion associated with the energy and angular momentum of the particle, respectively.

Then, focusing on the photons ($\mu=0$), we obtain four first-order differential equations for geodesic motion:

$$\dot{t}=\frac{\chi(L_z-E\chi)}{\Sigma\sin^2\vartheta}+\frac{(\Sigma+a\chi)((\Sigma+a\chi)E-aL_z)}{\Sigma\Delta_r}, \tag{10}$$

$$\dot{\varphi}=\frac{(L_z-E\chi)}{\Sigma\sin^2\vartheta}+\frac{a(E(a\chi+\Sigma)-aL_z)}{\Sigma\Delta_r}, \tag{11}$$

$$\Sigma^2\dot{\vartheta}^2=K-\frac{(E\chi-L_z)^2}{\sin^2\vartheta}=:\Theta(\vartheta), \tag{12}$$

$$\Sigma^2\dot{r}^2=((\Sigma+a\chi)E-aL_z)^2-\Delta_rK=:R(r), \tag{13}$$

where K is the Carter constant. Instead of the complete solution to the above equations, we are more interested in the photon region, which is filled by the null geodesics with

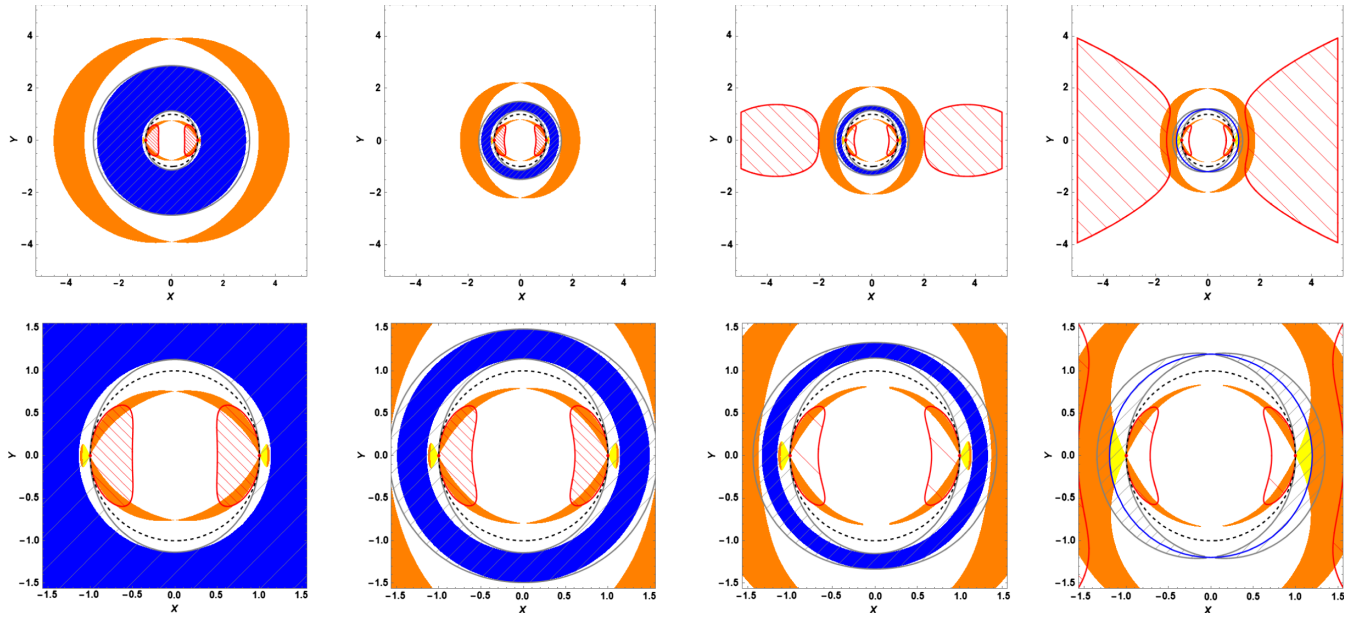

FIG. 4. Photon regions with $a = 0.5$, accompanied by the unidirectional membrane region, the ergosphere region, and the causality-violation region. The bottom plots show magnified versions of the inner parts of the upper plots.

circuit orbits. For convenience, we introduce the abbreviations

$$L_E \equiv \frac{L_z}{E}, \qquad K_E \equiv \frac{K}{E^2}. \tag{14}$$

Spherical orbits require $\dot{r} = 0$ and $\ddot{r} = 0$, which can be fulfilled by $R(r) = 0$ and $R'(r) = 0$ according to Eq. (13). Subsequently, the constants of motion K_E and L_E are given as

$$K_E = \frac{16r^2\Delta_r}{(\Delta_r')^2}, \qquad aL_E = (\Sigma + a\chi) - \frac{4r\Delta_r}{\Delta_r'}, \tag{15}$$

where a prime denotes a derivative to r. Substituting the above expression into Eq. (12), we find that its nonnegativity can give the condition for the photon region,

$$(4r\Delta_r - \Sigma\Delta_r')^2 \leq 16a^2r^2\Delta_r\sin^2\vartheta. \tag{16}$$

In this region, for each point with coordinates (r_p, ϑ_p), there is a null geodesic that stays on the sphere $r = r_p$, along which ϑ can oscillate between the extremal values determined by the equality in Eq. (16), while φ is governed by Eq. (11). With respect to radial perturbations, the spherical null geodesic at $r = r_p$ can be either unstable or stable depending on the sign of $R''(r_p)$, which can be derived from Eqs. (13) and (15) as

$$\frac{R''(r)}{8E^2}(\Delta_r')^2 = 2r\Delta_r\Delta_r' + r^2(\Delta_r')^2 - 2r^2\Delta_r\Delta_r''. \tag{17}$$

The condition $R''(r_p) > 0$ indicates that the spherical null geodesic is unstable, while $R''(r_p) < 0$ indicates that it is stable.

The photon regions of a charged rotating black hole in conformal gravity are shown in the (r, ϑ) plane in Figs. 4 and 5, where the unstable photon orbits (orange region) and stable photon orbits (yellow region) are distinguished. Here to cover all the cases including $r > 0$, $r = 0$, and $r < 0$, we shall use two different scales, following Ref. [75]. The radial coordinate is scaled as $m\exp(r/m)$ in the region $r < 0$ and as $r + m$ in the region $r > 0$; hence we use the black dashed circle to denote the throat at $r = 0$. Moreover, the blue region represents $\Delta r \leq 0$ and its boundaries indicate the black hole horizons. The upward- and downward-banded regions represent the ergosphere and the causality-violating regions, respectively. The red dot indicates the singularity.

In the figures, we fix $a = 0.5$ and 0.95, respectively, and change $\beta = \sharp\beta_{\rm ex}$, where $\sharp \in (0, 0.3, 0.6, 1)$ and $\beta_{\rm ex}$ is the corresponding extremal value (5). As in a Kerr black hole [75], we see an exterior photon region outside the outer horizon and an interior photon region inside the inner horizon, which are symmetric with respect to the equatorial plane. All photon orbits are unstable in the exterior photon region, while there exist both stable and unstable orbits in the interior photon region. The exterior and interior photon regions grow as a increases, but shrink as β increases. Moreover, the dependences of the unidirectional membrane region and the ergosphere region on the black hole parameters are also obvious and consistent with the analysis in the previous section. Also, the causality-violation region

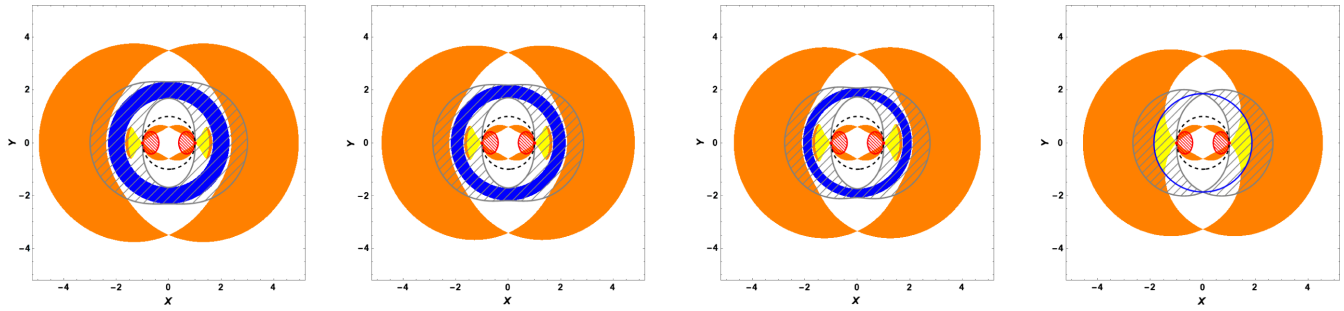

FIG. 5. Photon regions with $a = 0.95$, accompanied by the unidirectional membrane region, the ergosphere region, and the causality-violation region.

with negative r always exists, and for small a and large enough β we see an additional causality-violating region that is symmetric and extends from the outer horizon to a finite region depending on β.

IV. BLACK HOLE SHADOWS

Since the photon region determines the boundary of the black hole shadow, in this section we construct the shadow of the charged rotating black hole in conformal gravity.

A. Coordinates setup

For the light rays that issue from the position of an observer into the past, the initial direction is determined by two angles in the observer's sky: a colatitude angle and an azimuthal angle. Then, we consider an observer at position (r_o, ϑ_o) in Boyer-Lindquist coordinates. To fix the boundary of shadow, we choose the orthonormal tetrad [75]

$$e_0 = \left.\frac{(\Sigma + a\chi)\partial t + a\partial\varphi}{\sqrt{\Sigma\Delta r}}\right|_{(r_o,\vartheta_o)}, \qquad e_1 = \sqrt{\frac{1}{\Sigma}}\partial\vartheta|_{(r_o,\vartheta_o)},$$
$$e_2 = -\left.\frac{\partial\varphi + \chi\partial t}{\sqrt{\Sigma}\sin\vartheta}\right|_{(r_o,\vartheta_o)}, \qquad e_3 = -\sqrt{\frac{\Delta_r}{\Sigma}}\partial r|_{(r_o,\vartheta_o)} \tag{18}$$

at the observation event in the domain of outer communication. In this tetrad set, e_0 is to be interpreted as the four-velocity of our observer. For this observer, e_3 gives the spatial direction towards the center of the black hole. In addition, $e_0 \pm e_3$ are tangential to the principle null congruences of our metric. In this way, a linear combination of e_i is tangent to a light ray $s(\lambda) = (t(\lambda), r(\lambda), \vartheta(\lambda), \varphi(\lambda))$, such that we have

$$\partial_\lambda = \dot{r}\partial_r + \dot{\vartheta}\partial_\vartheta + \dot{\varphi}\partial_\varphi + \dot{t}\partial_t$$
$$= \alpha_s(-e_0 + \sin\theta\cos\psi e_1 + \sin\theta\sin\psi e_2 + \cos\theta e_3), \tag{19}$$

where the scalar factor can be determined by inserting Eq. (18) into Eq. (19) as

$$\alpha_s = \left.\frac{aL_z - (\Sigma + a\chi)E}{\sqrt{\Sigma\Delta_r}}\right|_{(r_o,\vartheta_o)}, \tag{20}$$

and it is easy to see that the direction $\theta = 0$ points to the black hole. Moreover, here we have introduced θ and ψ which are the aforementioned two angles, i.e., the celestial coordinates in the observer's sky; see the left panel of Fig. 6. Further comparing the coefficients of ∂_t and ∂_r, we find that

$$\sin\psi = \left.\frac{L_E - \chi}{\sqrt{K_E}\sin\vartheta}\right|_{\vartheta=\vartheta_o}, \qquad \sin\theta = \left.\frac{\sqrt{\Delta_r K_E}}{\Sigma + a\chi - aL_E}\right|_{r=r_o}. \tag{21}$$

Since the boundary of the shadow could correspond to the light rays which asymptotically approach a spherical null geodesic, so such light ray must have the same K_E and L_E as the limiting spherical null geodesic. Therefore, recalling Eq. (21), we have

$$K_E = \left.\frac{16r^2\Delta_r}{(\Delta_r')^2}\right|_{r=r_p}, \qquad aL_E = (\Sigma + a\chi) - \left.\frac{4r\Delta_r}{\Delta_r'}\right|_{r=r_p}, \tag{22}$$

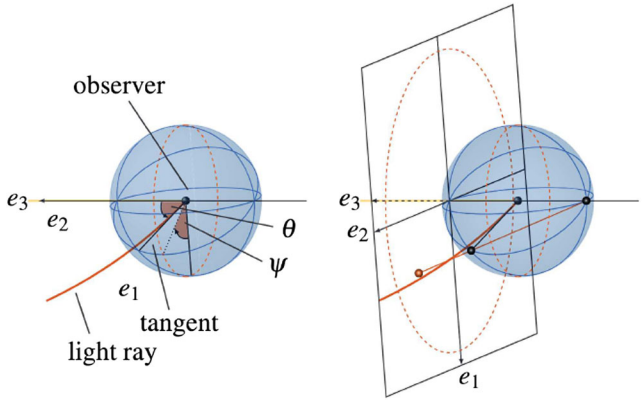

FIG. 6. These figures are taken from Ref. [55]. The left panel shows the definition of the celestial coordinates θ and ψ on the observer's sky. The right panel shows the stereographic projection of the celestial sphere onto a plane.

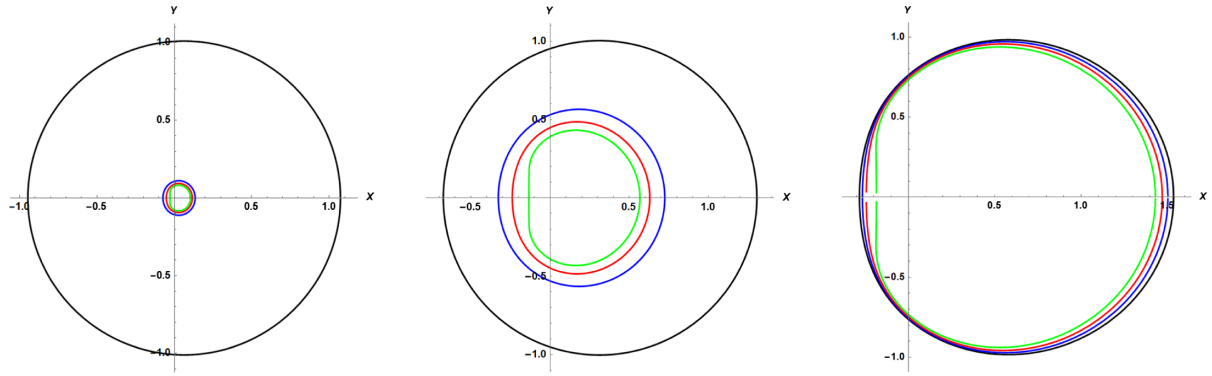

FIG. 7. Black hole shadows seen by an equatorial observer ($\vartheta_o = \frac{\pi}{2}$) at $r_o = 5$. Plots from left to right correspond to $a = 0.1$, $a = 0.5$, and $a = 0.95$. In each plot the black, blue, red, and green curves correspond to $\beta = (0, 0.3, 0.6, 0.999)\beta_{\rm ex}$.

where r_p is the radius coordinate of the limiting spherical null geodesic.

Therefore, the boundary of the black hole shadow depends on r_p in the form of $(\theta(r_p), \psi(r_p))$. Since the points (θ, ψ) and $(\theta, \pi - \psi)$ have the same K_E and L_E, the shadow is symmetric with respect to the horizontal axis. For $a > 0$, θ reaches its maximum and minimum values along the boundary curve at $\psi = -\pi/2$ and $\psi = \pi/2$, respectively, which give us the corresponding $r_p^{\rm max}$ and $r_p^{\rm min}$. Putting Eq. (22) into Eq. (21) with $\psi = \mp\,\pi/2$, $r_p^{\rm max\,/\,min}$ can be solved via

$$(4r\Delta_r - \Sigma\Delta_r') \mp 4ar\sqrt{\Delta_r}\sin\vartheta|_{(r=r_p,\vartheta=\vartheta_o)} = 0. \quad (23)$$

Note that for $a = 0$, the above method that parametrizes the shadow boundary by r_p does not work.

Then, following Ref. [75], we can apply the stereographic projection (see the right panel of Fig. 6) to transform the celestial coordinates $(\theta(r_p), \psi(r_p))$ into the standard Cartesian coordinates $(X(r_p), Y(r_p))$,

$$X(r_p) = -2\tan\left(\frac{\theta(r_p)}{2}\right)\sin\psi(r_p),$$
$$Y(r_p) = -2\tan\left(\frac{\theta(r_p)}{2}\right)\cos\psi(r_p). \quad (24)$$

Then we can figure out the boundary of the shadow on a two-dimensional plane, observed by our chosen observer with four-velocity e_0. Note that the range of the inclination angle is $\vartheta_o \in [0, \pi]$, and $\vartheta_o = 0(\pi)$ corresponds to an observer in the north (south) direction while $\vartheta_o = \pi/2$ corresponds to an observer in the equatorial plane of the black hole. Due to the symmetry, we consider $\vartheta_o \in [0, \pi/2]$ in the following.

B. Shadow for observers at finite distance

First, we consider an observer located at a finite distance with position (r_o, ϑ_o). We know that for a nonrotating black hole the shape of the shadow is a perfect circle due to the spherically symmetry if the system, and rotation will deform this shape. In Figs. 7 and 8 we show the boundary of the shadow for a charged rotating black hole in conformal gravity.

The effects of the parameter β with different values of a are shown in Fig. 7. It is clear that both a and β enhance the deformation of the shadow. This means that the shadow of the charged rotating black hole in conformal gravity with parameters (a, β) and that of the Kerr black hole with a certain spin may be coincident. The influence of the charge parameter β in conformal gravity on the shadow is qualitatively similar to that of the KN case [55,75–77]. In Fig. 8 we fix $a = 0.95$ and $\beta = 0.999\beta_{\rm ex}$. The left panel shows the influence of the viewing angle of the observer, which indicates that the shadow remains circular for a polar observer with $\vartheta_o = 0$, while the shadow is maximally deformed for an observer in the equatorial plane with $\vartheta_o = \pi/2$. The right panel shows the influence of the distance between the observer and the black hole on the shadow, where the shadow is smaller for a farther observer, as expected.

V. SHADOW OBSERVABLES AND PARAMETER ESTIMATION

To carefully study how the shadow observables are affected by the model parameters, we consider black hole shadows observed at spatial infinity, i.e., $r_o \gg m$. In this case, as addressed in Ref. [55], the coordinates in Eq. (24) can be transformed to $\bar{\alpha} = r_o X - a\sin\vartheta_o$ and $\bar{\beta} = r_o Y$, which are derived as

$$\bar{\alpha}(r_p) = -\frac{\xi(r_p)}{\sin\vartheta_o},$$
$$\bar{\beta}(r_p) = \pm\sqrt{\eta(r_p) + a^2\cos^2\vartheta_o - \xi(r_p)^2\cot^2\vartheta_o}, \quad (25)$$

where $\xi(r_p) = L_E|_{r_p}$ and $\eta = K_E - (L_E - a)^2|_{r_p}$. Here $(\bar{\alpha}, \bar{\beta})$ are Bardeen's two impact parameters with dimension *[Length]* describing the celestial sphere [78].

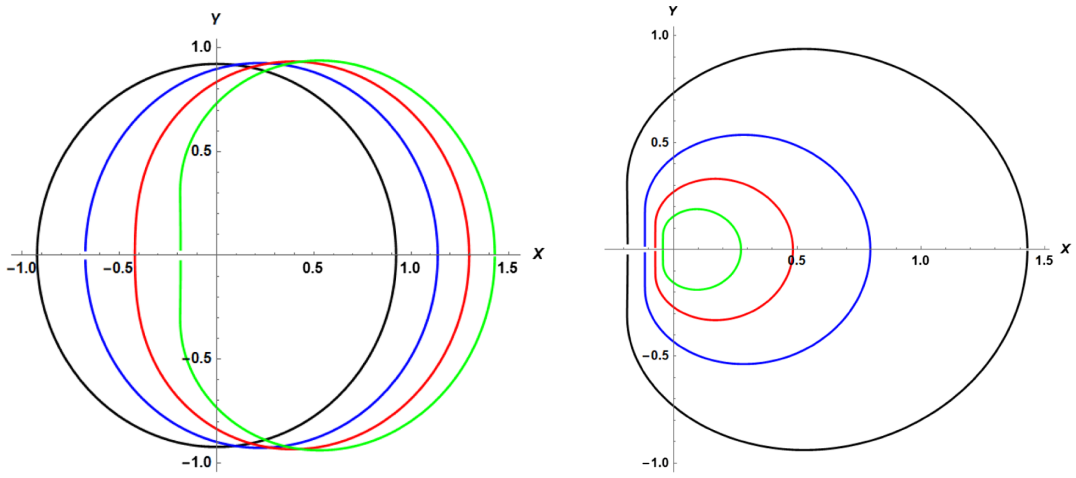

FIG. 8. Left: black hole shadows with $r_o = 5$ and different viewing angles. The shadow boundaries from left to right have $\vartheta_o = 0, \pi/8, \pi/4$, and $\pi/2$, respectively. Right: black hole shadows with $\vartheta_o = \pi/2$ and $r_o = 5$, 10, 20, 50 for boundaries from outer to inner. In both panels we fix $a = 0.95$ and $\beta = 0.999\beta_{\rm ex}$.

Subsequently, we show the boundary of the shadow for an observer at spatial infinity in Figs. 9 and 10, in which the axes labels (X, Y) represent $(\bar{\alpha}/m, \bar{\beta}/m)$. We see that the boundary of the black hole shadow closely depends on the parameters a, β, and ϑ_o, and the rules are similar as those in the case of which the observer is at finite distance. We note that the black hole parameters are expected to be associated and estimated from observations. Though the image of M87* is mostly connected with a Kerr black hole, our results show that the presence of additional parameter also leads to the distortion of the shadow. Thus, here we shall study how to estimate the black hole parameters from the shadow observables (shadow size and distortion), rather than simply describe the properties of shadow.

A. Shadow size and deformation

To describe the distortion and size of a charged rotating black hole in conformal gravity, we first study two characteristic observables, R_s and δ_s, which were proposed by Hioki and Maeda [32]. Here R_s is the radius of the reference circle for the distorted shadow and δ_s is the deviation of the left edge of the shadow from the reference circle boundary. For convenience, we denote the top, bottom, right, and left of the reference circle as (X_t, Y_t), (X_b, Y_b), $(X_r, 0)$, and $(X'_l, 0)$, respectively, and $(X_l, 0)$ is the leftmost edge of the shadow [79]. Subsequently, the definitions of the characteristic observables are [32]

$$R_s = \frac{(X_t - X_r)^2 + Y_t^2}{2|X_r - X_t|}, \qquad \delta_s = \frac{|X_l - X'_l|}{R_s}. \tag{26}$$

From the density plots of R_s and δ_s in Figs. 11 and 12, we see that the black hole parameters in the conformal gravity indeed affect the size and shape of the shadow. Figure 11 shows that with the increase of the charge parameter β, the radius R_s decreases rapidly. It is slightly affected by the spin parameter a and the inclination angle ϑ_o, and their effects are enlarged in the left panel of Fig. 13, from which we find that R_s slightly decreases as a increases

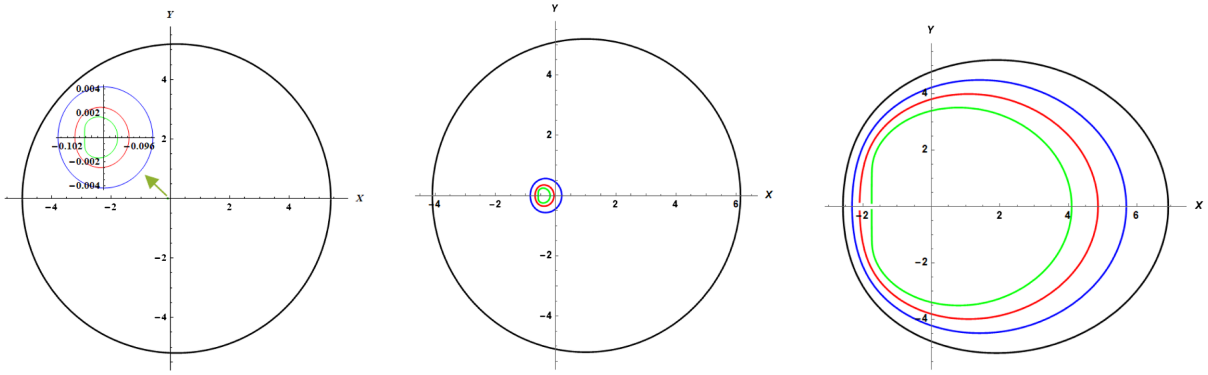

FIG. 9. Black hole shadow seen by an observer at infinite distance and $\vartheta_0 = \pi/2$. We fix $a = 0.1$, $a = 0.5$, and $a = 0.95$ from left to right. In each panel the black, blue, red, and green curves correspond to $\beta = (0, 0.3, 0.6, 0.999)\beta_{\rm ex}$.

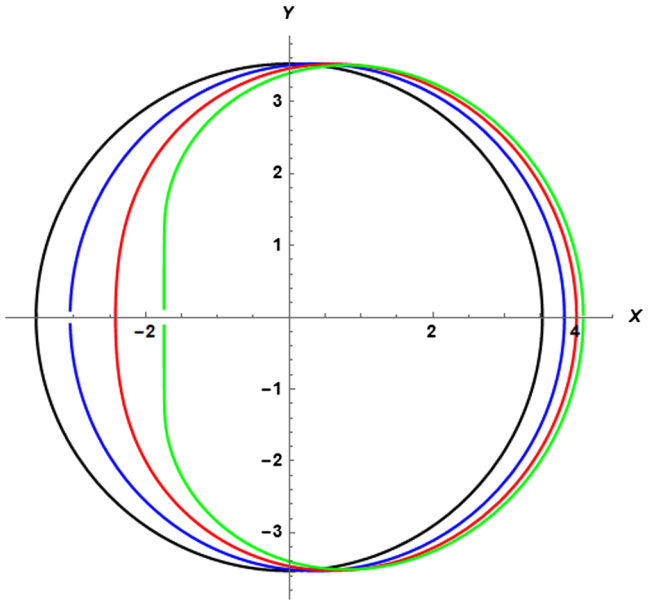

FIG. 10. Black hole shadows seen by an observer at infinite distance for different inclination angles: $\vartheta_o = 0$ (black), $\pi/8$ (blue), $\pi/4$ (red), and $\pi/2$ (green). We fix $a = 0.95$ and $\beta = 0.999\beta_{\rm ex}$.

while it increases as ϑ_o increases. On the other hand, Fig. 12 shows that by increasing a or ϑ_o, the distortion character δ_s increases which means that the shadow is more distorted, as expected. Moreover, when a or ϑ_o is small, the effect of β on δ_s is small, but when they are large enough, β has a profoundly incremental effect. The above analysis further implies that, compared to a Kerr black hole, the shadow radius of this charged rotating black hole in conformal gravity is always smaller but more distorted, which is similar to that of a KN black hole [48].

R_s and δ_s may not accurately describe the shadow of some irregular black holes as they require the shadow of black holes to have a certain symmetry. Then, to characterize shadows of any shape, Kumar and Ghosh proposed another two characteristic observables—the shadow area A and oblateness D—which are defined as [33]

$$A = 2\int Y(r_p)dX(r_p) = 2\int_{r_p^{\rm min}}^{r_p^{\rm max}} \left(Y(r_p)\frac{dX(r_p)}{dr_p}\right)dr_p,$$
$$D = \frac{X_r - X_l}{Y_t - Y_b}. \tag{27}$$

It was found in Ref. [37] that $D = 1$ for a Schwarzschild black hole and $\sqrt{3}/2 \le D < 1$ for a Kerr black hole as viewed by an equatorial observer, where $D = \sqrt{3}/2$ is for the extremal case. In Figs. 14 and 15 we show the density plots of A and D for the shadow of a charged rotating black hole in conformal gravity. The area A monotonously decreases as β increases. The influence of a and ϑ_o is enlarged in the right panel of Fig. 13, which shows that the area slightly decreases as the spin increases while the effect of ϑ_o is negligible. As β increases, the oblateness D becomes smaller which is significant near the extremal case. In addition, as a or ϑ_o increases with the other fixed, D also has decremental tendency. The above analysis also implies that the shadow of a charged rotating black hole in conformal gravity is smaller and more distorted than that of a Kerr black hole, which matches our aforementioned finding.

So far, we have explored how the black hole parameters influence the two couples of shadow observables, i.e., (R_s, δ_s) and (A, D). Then, with given values of (R_s, δ_s) or (A, D), we can find their contour intersection in the a-β plane to estimate the parameters of a charged rotating black hole in conformal gravity. This method of black hole parameter estimation from its shadow observables was implemented in Refs. [32,33,47,53]. Here, we fix $\vartheta_o = \pi/2$ and show the contour plots of R_s and δ_s as well as A and D in Fig. 16, in which the intersection point of $R_s(A)$ and

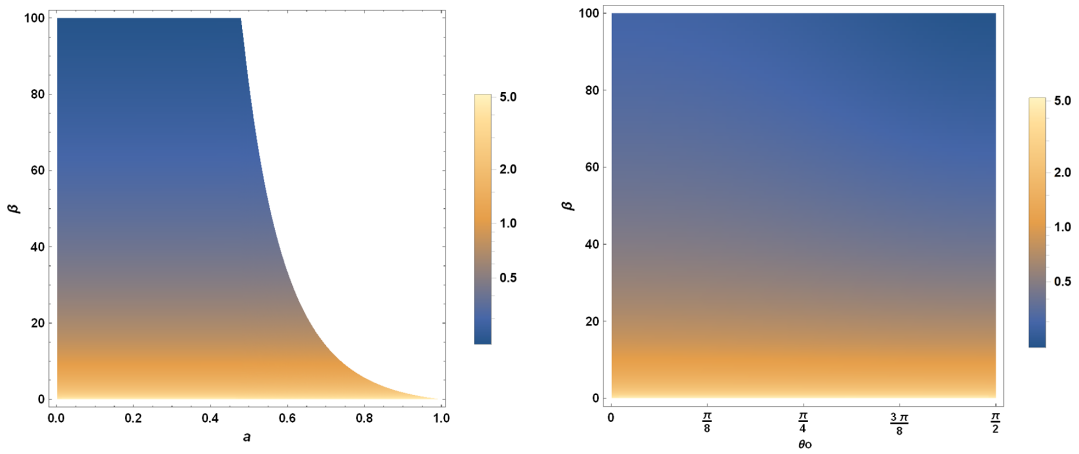

FIG. 11. Density plots for the radius of the reference circle R_s as a function of a and β. Here we fix $\vartheta_o = \pi/2$ in the left panel and $a = 0.4$ in the right panel.

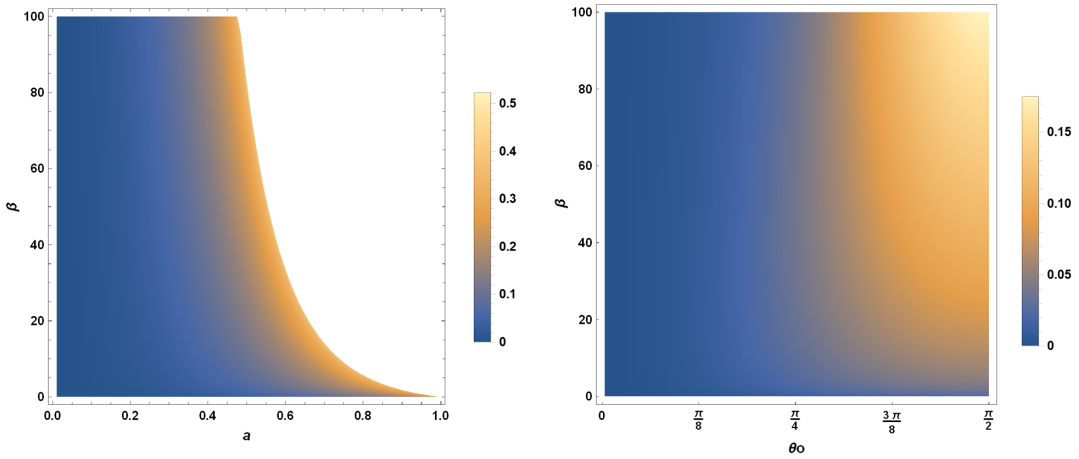

FIG. 12. Density plot of the distortion δ_s. Here we fix $\vartheta_o = \pi/2$ in the left panel and $a = 0.4$ in the right panel.

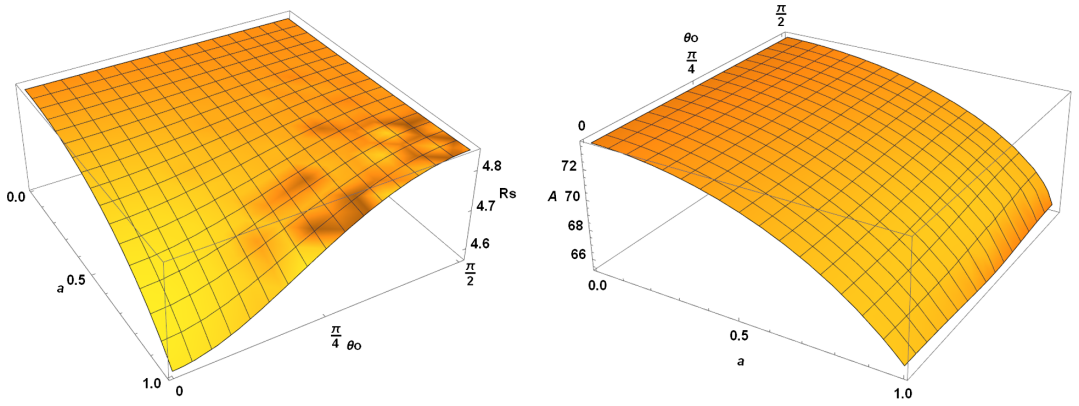

FIG. 13. Three-dimensional plots of radius R_s (left) and area A (right) of the black hole shadow. Here we fix $\beta = 0.1$.

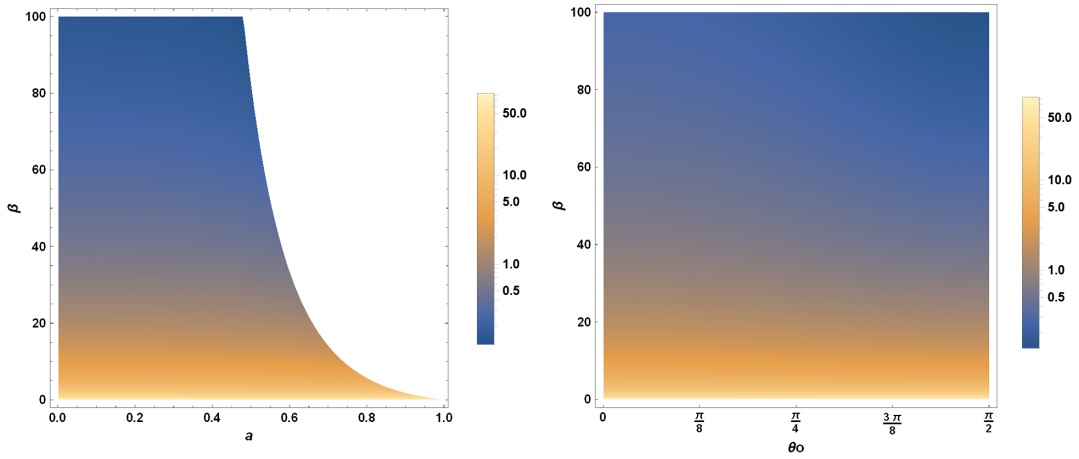

FIG. 14. Density plots of the shadow area A. Here we fix $\vartheta_o = \pi/2$ in the left panel and $a = 0.4$ in the right panel.

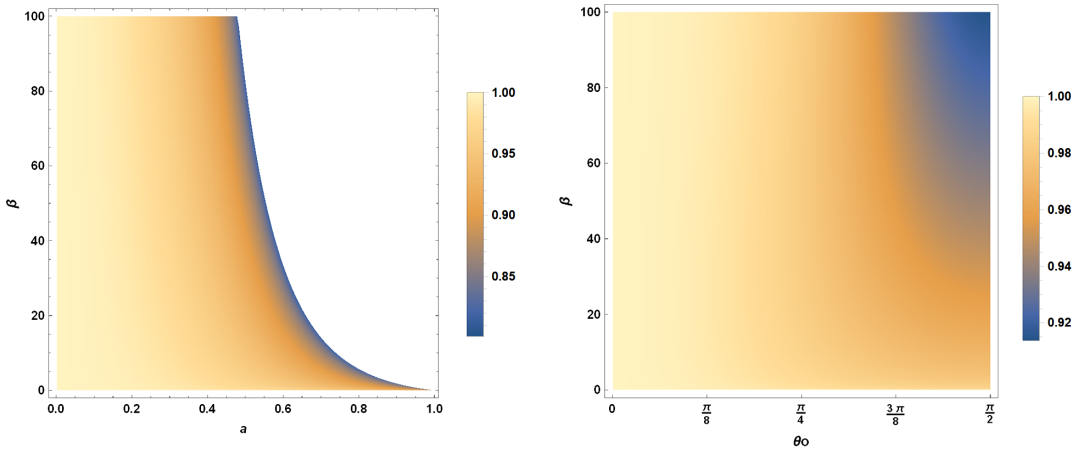

FIG. 15. Density plots of the oblateness D. Here we fix $\vartheta_o = \pi/2$ in the left panel and $a = 0.4$ in the right panel.

$\delta_s(D)$ uniquely determines the black hole parameters a and β.

B. Energy emission rate

Apart from being used to estimate the model parameters, the shadow observables are also helpful to predict various interesting astronomical phenomena [33,39,47]. In this subsection we analyze the energy emission rate for a charged rotating black hole in conformal gravity using the shadow observables. For an observer at infinite distance, the shadow of a spherically symmetric black hole coincides with a high-energy absorption cross section, which oscillates around a constant limiting value $\delta_{\rm lim}$. It was addressed in Ref. [35] that $\delta_{\rm lim}$ is connected to the black hole shadow via

$$\delta_{\rm lim} \approx \pi R_s^2, \tag{28}$$

with R_s defined in Eq. (26); hence, the energy emission rate for a rotating black hole can be calculated as

$$\frac{d^2E(\varpi)}{d\varpi dt} = \frac{2\pi^2 R_s^2}{e^{\varpi/T} - 1}\varpi^3, \tag{29}$$

where ϖ is the photon frequency and T is the Hawking temperature at the event horizon of the black hole.

The energy emission rate in this proposal has been widely studied in GR and MG. Now we intend to discuss the energy emission rate for the charged rotating black hole (2), the Hawking temperature of which is

$$T = \frac{-6a^2 + \sqrt{9(a^2 + r_+^2)^2 + 12r_+^4\beta}}{12\pi r_+(a^2 + r_+^2)}. \tag{30}$$

In Fig. 17 we present the behavior of the energy emission rate as a function of photon frequency. The left and middle

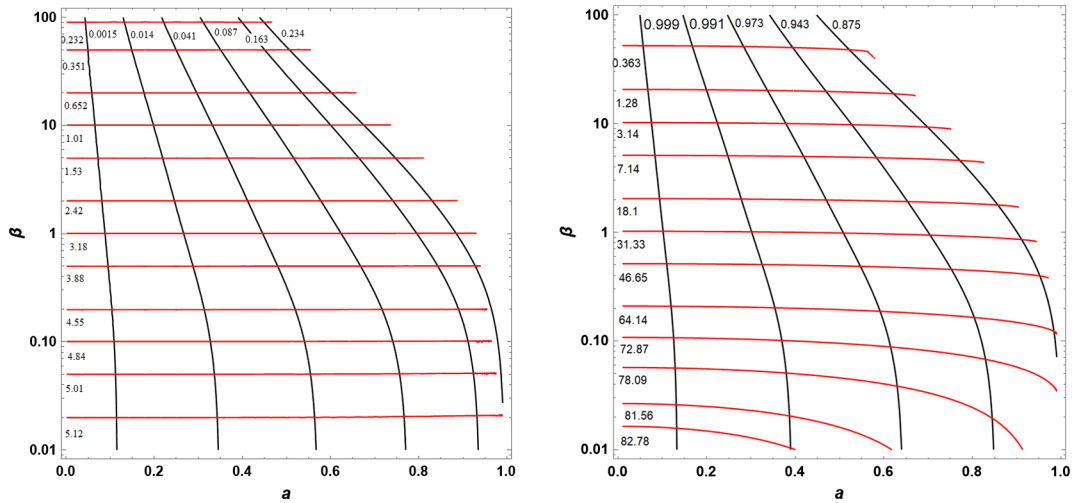

FIG. 16. Left: the contour plot for shadow observables R_s (red) and δ_s (black) in the parameter plane (a, β) of a charged rotating black hole in conformal gravity. Right: the contour plot for shadow observables A (red) and D (black).

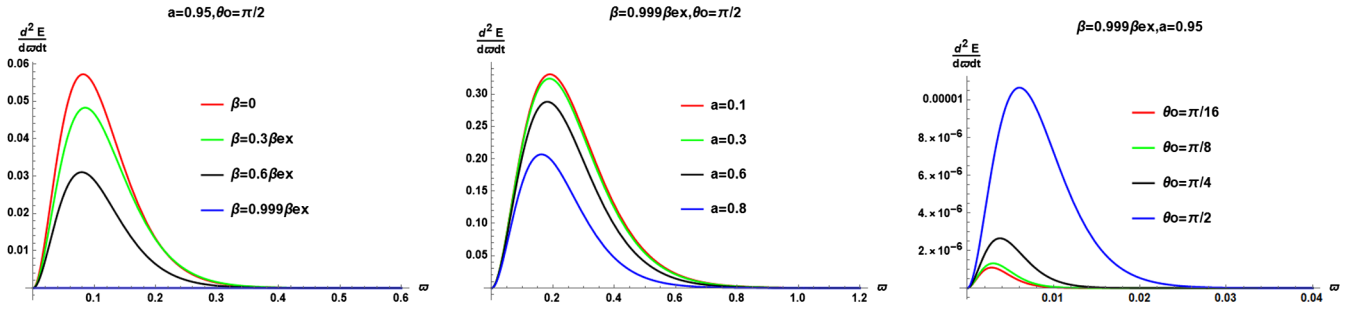

FIG. 17. Distribution of the energy emission rate in terms of the photon frequency ϖ with various values of the parameters β, ϑ_o, and a.

panels show that the peak of the emission rate decreases as both β and a increase and the peak shifts to lower frequency, while the right panel shows that the inclination angle has the opposite effect on the emission rate.

VI. CONSTRAINTS FROM EHT OBSERVATIONS OF M87*

The black hole image of M87* photographed by the EHT Collaboration is crescent shaped, and its deviation from circularity in terms of the root-mean-square distance from the average radius of the shadow is $\Delta C \lesssim 0.1$. The axis ratio is $1 < D_x \lesssim 4/3$ and the angular diameter is $\theta_d = 42 \pm 3\ \mu$as [56–58]. The preliminary analysis of the image of M87* taken by the EHT Collaboration referred to a Kerr black hole whose parameters are constrained by the above observations, but the results cannot rule out the alternative black holes in GR or the rotating black holes in MG. Thus, the shadow observables ΔC, D_x, and θ_d can also be used to constrain the parameters of black holes in MG, and some attempts can be seen in Refs. [47–53,59–62].

In this section we presuppose that M87* is a rotating charged black hole in conformal gravity and use the EHT observations to constrain the parameters a and β. To this end, we first review the definitions of ΔC, D_x, and θ_d, and show their density plots in the parameter space (a, β).

To describe the circularity deviation ΔC, we have to recall from Sec. V A that a distorted black hole shadow is always compared to a reference circle. The geometric center of the shadow (X_c, Y_c) is connected with the edges of the shaped boundary via $(X_c = \frac{X_r + X_l}{2}, Y_c = 0)$, and with this point as the origin, the boundary of a black hole shadow can be described by the polar coordinates $(\phi, R(\phi))$, where

$$\phi = \tan^{-1}\left(\frac{Y - Y_C}{X - X_c}\right), \qquad R(\phi) = \sqrt{(X - X_c)^2 + (Y - Y_c)^2}, \tag{31}$$

while the average radius of the shadow is

$$\bar{R} = \frac{1}{2\pi}\int_0^{2\pi} R(\phi) d\phi. \tag{32}$$

Then, the circularity deviation ΔC, which measures the deviation from a perfect circle, is defined by [47]

$$\Delta C = \frac{1}{\bar{R}}\sqrt{\frac{1}{2\pi}\int_0^{2\pi}(R(\phi) - \bar{R})^2 d\phi}. \tag{33}$$

The axis ratio is given by [15]

$$D_x = \frac{1}{D} = \frac{Y_t - Y_b}{X_r - X_l}, \tag{34}$$

where the oblateness D has been defined in Eq. (27). In fact, D_x can be seen as another way of defining the circular derivation since the emission ring reconstructed in the EHT images is close to circular with an axial ratio of 4:3, which indeed also corresponds to $\Delta C \lesssim 0.1$ [56].

Another observable from the EHT Collaboration is the angular diameter of the shadow, which is defined as [39]

$$\theta_d = 2\frac{R_a}{d}, \tag{35}$$

where $R_a = \sqrt{\frac{A}{\pi}}$ [with A defined in Eq. (27)] is known as the shadow areal radius and d is the distance of M87* from the Earth.

It is obvious from Eqs. (33), (34), and (35) that ΔC, D_x, and θ_d depend on the black hole parameters. Assuming that M87* is a charged rotating black hole in conformal gravity, we can evaluate them for the metric (2) and use the EHT observations $\Delta C \lesssim 0.1$, $D_x \in (1, 4/3]$ and $\theta_d \in [39, 45]\,\mu as$ to give constraints on the parameters a and β. In addition, we know that the shadow is maximally deformed at large inclination angle $\vartheta_o = \pi/2 = 90°$, while the inclination angle (with respect to the line of sight) is estimated to be $\vartheta_o = 17°$ in the M87* image if considering the orientation of the relativistic jets [80]. Thus, we show our computational results for both $\vartheta_o = 90°$ and $\vartheta_o = 17°$.

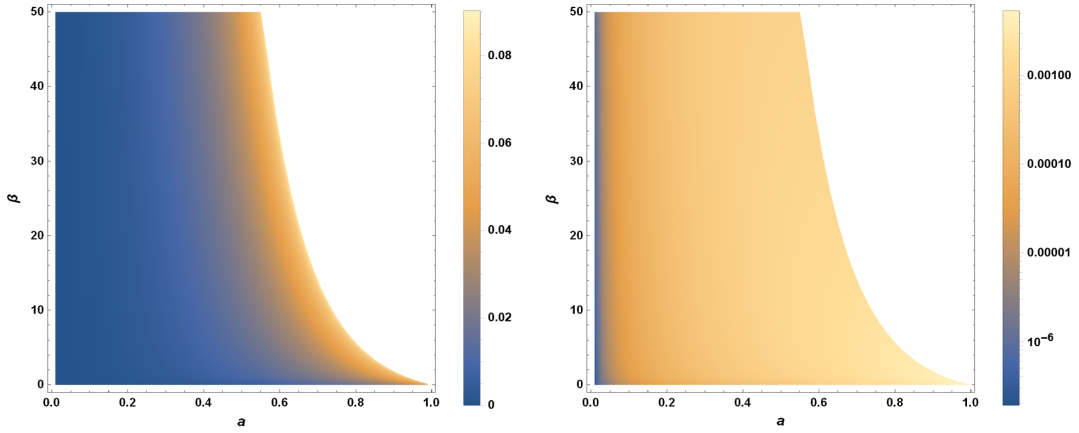

FIG. 18. Density plots of the circularity deviation ΔC. The left panel is for $\vartheta_o = 90°$ while the right panel is for $\vartheta_o = 17°$.

We give the density plots of the circularity deviation ΔC in Fig. 18, which shows that the shadows of a charged rotating black hole in conformal gravity satisfy $\Delta C \lesssim 0.1$ for all theoretically allowed parameters. Moreover, we also show the density plots of D_x in Fig. 19. We see that for the entire parameter space, the axial ratio is within the observational constraint $D_x \in (1, 4/3]$, which is consistent with the conclusion from $\Delta C \lesssim 0.1$, as expected. In addition, in order to compare with $D_x \in (1, 2\sqrt{3}/3]$ in a Kerr black hole, we show the contour with $D_x = 2\sqrt{3}/3$ in the calculation. For $\vartheta = 90°$, we see that in the current background, although all parameters satisfy $D_x < 4/3$, there is still some portion of parameter space with $D_x > 2\sqrt{3}/3$. This means that in the future, if the EHT experiment is precise enough to constrain $2\sqrt{3}/3 < D_x < 4/3$, then it can exclude a Kerr black hole at the center of M87* but cannot exclude a charged rotating black hole in conformal gravity. Nevertheless, for $\vartheta = 17°$, all of the parameters give $1 < D_x \leq 2\sqrt{3}/3$, so one cannot distinguish GR and conformal gravity.

In Fig. 20 we present the density plots of θ_d for a charged rotating black hole in conformal gravity. In the calculation, we set $d = 16.8$ Mpc and the black hole mass is $m = 6.5 \times 10^9\ M_\odot$ as estimated by the EHT Collaboration. The enlarged plots in the right panel clearly show that only the parameter space in the left corner enclosed by the $\theta_d = 39\ \mu$as contour (the black curve) is consistent with the EHT observations of M87*, indicating that θ_d gives an upper limit on both a and β in a charged rotating black hole in conformal gravity [Eq. (2)]. Moreover, it is not difficult to find that the constraint on a at $\vartheta = 17°$ is stricter than that at $\vartheta = 90°$, but the difference of their effects on β is small.

VII. CLOSING REMARKS

The EHT observations on the image of black hole are consistent with the predictions from Kerr black hole in GR, but the observations cannot rule out either the alternative to the Kerr black hole or black holes in other theories of gravity. In this paper, we considered a charged rotating black hole in conformal gravity which has remarkable applications in cosmological and holographical framework.

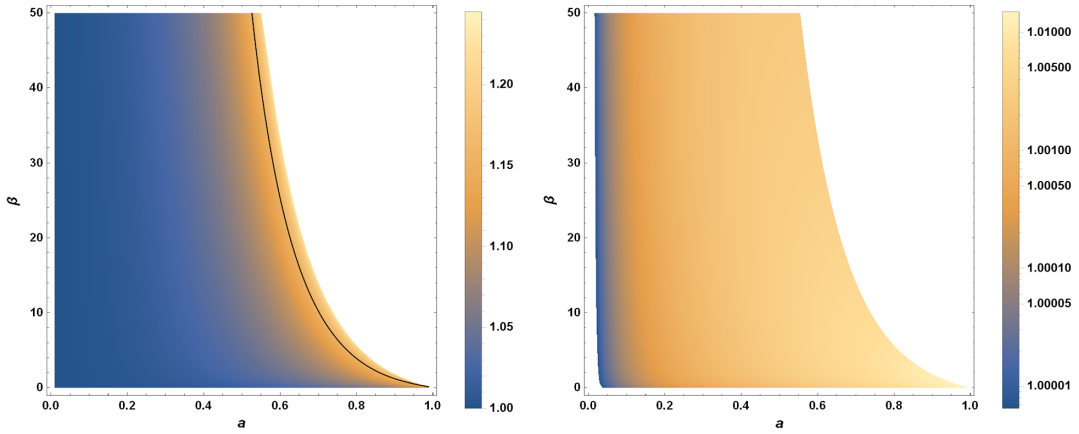

FIG. 19. Density plots of the axial ratio D_x. The left panel is for $\vartheta_o = 90°$ while the right panel is for $\vartheta_o = 17°$. The black curve in the left panel denotes the $D_x = 2\sqrt{3}/3$ contour which is the upper bound for a Kerr black hole.

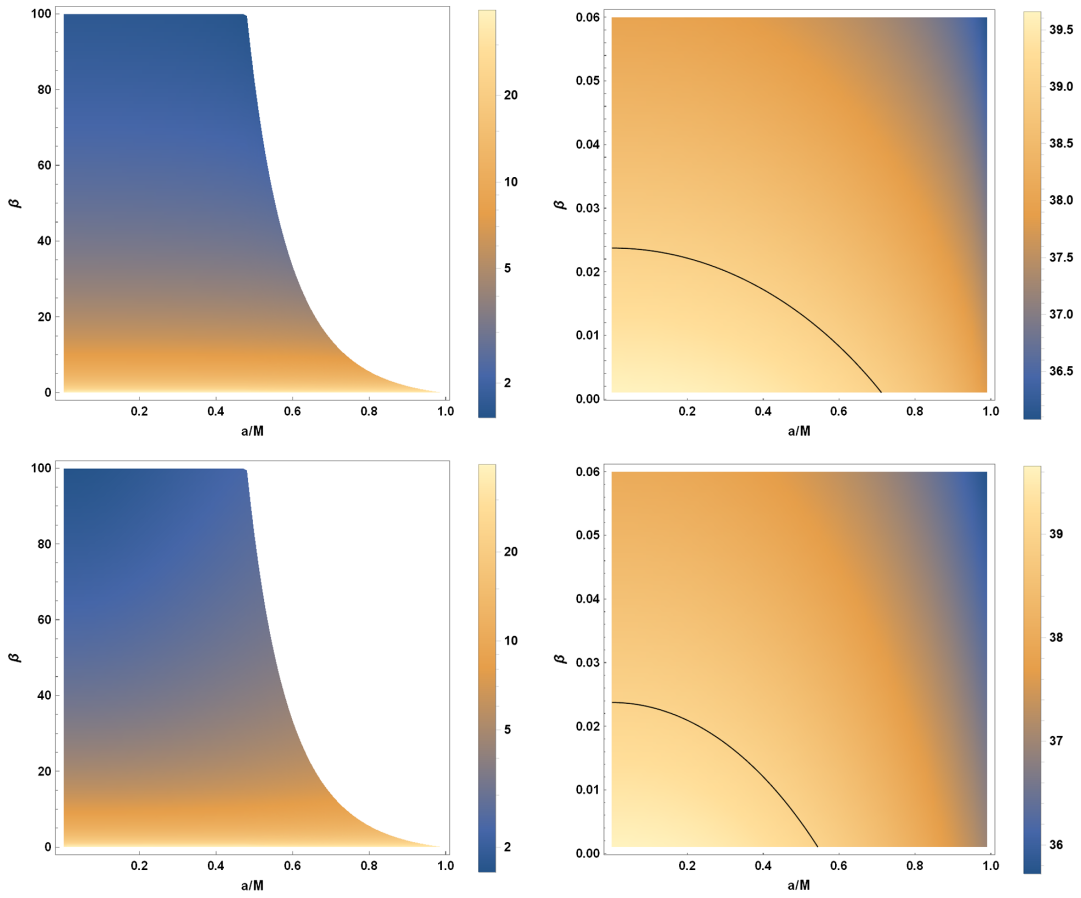

FIG. 20. Density plots of the angular diameter θ_d. The upper panels are for $\vartheta_o = 90°$ while the bottom panels are for $\vartheta_o = 17°$. The black curves in the right enlarged plots correspond to $\theta_d = 39$ μas.

The charge related term in the current black hole has a different falloff than that in a KN black hole, such that it exhibits different configurations. The charge parameter β would decrease the size of both the Cauchy and event horizons, of which the tendency is similar to that in a KN black hole but with a different slope. Also, the size of the event horizon in the extremal case decreases as the charge parameter increases, in contrast to the independent situation in a KN black hole. Moreover, the falloff term also has an influence on the static limit surfaces, ergoregions, the causality-violating regions, and photon regions, as we explicitly presented in Figs. 4 and 5.

Then, we figured out the shadow boundary of the black hole with various cases for observers at both finite and infinite distances. The effects of the spin parameter, the charge parameter, the inclination angle, and the distance on the shadow shape can be clearly seen in Figs. 7–10, which are qualitatively similar to that of a Kerr or KN black hole [75,81,82]. Then, focusing on the shadow cast for an observer at infinity, we systematically analyzed the shadow observables that characterize the shadow size and shape, namely, the shadow radius R_s, distortion δ_s, shadow area A, and oblateness D. We found that, compared with a Kerr black hole, the black hole shadow is smaller and more distorted as the charge parameter increases. Our analysis also indicates that the shadow observables can be used to estimate the parameters (a, β) of a charged rotating black hole in conformal gravity.

Finally, we considered M87* as observed by the EHT experiment as a charged rotating black hole in conformal gravity, and used the EHT constraints on the circularity deviation ΔC, the axial ratio D_x, and the angular diameter θ_d to constrain the black hole parameters. For inclination angles $\vartheta_0 = 90°$ and $\vartheta_0 = 17°$, the entire (a, β) space satisfies $\Delta C \lesssim 0.1$ and $1 < D_x \lesssim 4/3$. It is worth pointing out that for $\vartheta = 90°$, a portion of the parameter space gives $2\sqrt{3}/3 < D_x < 4/3$, where $D_x = 2\sqrt{3}/3$ is the upper bound for a Kerr black hole. However, for $\vartheta = 17°$, all of the parameters give $1 < D_x < 2\sqrt{3}/3$, so one cannot distinguish GR and conformal gravity in this case. 39 μas $\leq \theta_d \leq 45$ μas gives upper bounds on both a and β and constrains the parameter space into a small portion. To conclude, for charged rotating black hole, there exists plenty of parameter groups (a, β) of which the black hole shadow are consistent with that in EHT observations of M87*.

Our findings indicate that charged rotating black holes in conformal gravity with these parameters could be candidates for astrophysical black holes. Moreover, for an equatorial observer, the EHT constraint on the axial ratio D_x could help to distinguish a Kerr black hole and a charged rotating black hole in conformal gravity in some parameter space.

ACKNOWLEDGMENTS

We appreciate Xi-Jing Wang for helpful discussion. This work is partly supported by Fok Ying Tung Education Foundation under Grant No. 171006 and Natural Science Foundation of Jiangsu Province under Grant No. BK20211601.

[1] J. M. Bardeen, *Les Houches Summer School of Theoretical Physics: Black Holes* (Gordon and Breach Science Publishers, Inc., United States, 1973), pp. 215–240.
[2] J. L. Synge, The escape of photons from gravitationally intense stars, Mon. Not. R. Astron. Soc. **131**, 463 (1966).
[3] H. Falcke, F. Melia, and E. Agol, Viewing the shadow of the black hole at the galactic center, Astrophys. J. Lett. **528**, L13 (2000).
[4] K. S. Virbhadra and G. F. R. Ellis, Schwarzschild black hole lensing, Phys. Rev. D **62**, 084003 (2000).
[5] Z. Q. Shen, K. Y. Lo, M. C. Liang, P. T. P. Ho, and J. H. Zhao, A size of ~1 au for the radio source Sgr a* at the centre of the Milky Way, Nature (London) **438**, 62 (2005).
[6] P. V. P. Cunha, C. A. R. Herdeiro, E. Radu, and H. F. Runarsson, Shadows of Kerr Black Holes with Scalar Hair, Phys. Rev. Lett. **115**, 211102 (2015).
[7] Z. Younsi, A. Zhidenko, L. Rezzolla, R. Konoplya, and Y. Mizuno, New method for shadow calculations: Application to parametrized axisymmetric black holes, Phys. Rev. D **94**, 084025 (2016).
[8] F. Atamurotov, A. Abdujabbarov, and B. Ahmedov, Shadow of rotating non-Kerr black hole, Phys. Rev. D **88**, 064004 (2013).
[9] F. Atamurotov, S. G. Ghosh, and B. Ahmedov, Horizon structure of rotating Einstein–Born–Infeld black holes and shadow, Eur. Phys. J. C **76**, 273 (2016).
[10] M. Amir, B. P. Singh, and S. G. Ghosh, Shadows of rotating five-dimensional charged EMCS black holes, Eur. Phys. J. C **78**, 399 (2018).
[11] E. F. Eiroa and C. M. Sendra, Shadow cast by rotating braneworld black holes with a cosmological constant, Eur. Phys. J. C **78**, 91 (2018).
[12] S. Vagnozzi and L. Visinelli, Hunting for extra dimensions in the shadow of M87*, Phys. Rev. D **100**, 024020 (2019).
[13] F. Long, J. Wang, S. Chen, and J. Jing, Shadow of a rotating squashed Kaluza-Klein black hole, J. High Energy Phys. 10 (2019) 269.
[14] F. Long, S. Chen, M. Wang, and J. Jing, Shadow of a disformal Kerr black hole in quadratic degenerate higher-order scalar–tensor theories, Eur. Phys. J. C **80**, 1180 (2020).
[15] I. Banerjee, S. Chakraborty, and S. SenGupta, Silhouette of M87*: A new window to peek into the world of hidden dimensions, Phys. Rev. D **101**, 041301 (2020).
[16] A. K. Mishra, S. Chakraborty, and S. Sarkar, Understanding photon sphere and black hole shadow in dynamically evolving spacetimes, Phys. Rev. D **99**, 104080 (2019).
[17] R. Kumar, S. G. Ghosh, and A. Wang, Gravitational deflection of light and shadow cast by rotating Kalb-Ramond black holes, Phys. Rev. D **101**, 104001 (2020).
[18] W. L. Qian, S. Chen, C. G. Shao, B. Wang, and R. H. Yue, Cuspy and fractured black hole shadows in a toy model with axisymmetry, Eur. Phys. J. C **82**, 91 (2022).
[19] X. X. Zeng, H. Q. Zhang, and H. Zhang, Shadows and photon spheres with spherical accretions in the four-dimensional Gauss–Bonnet black hole, Eur. Phys. J. C **80**, 872 (2020).
[20] X. X. Zeng, G. P. Li, and K. J. He, The shadows and observational appearance of a noncommutative black hole surrounded by various profiles of accretions, Nucl. Phys. **B974**, 115639 (2022).
[21] F. L. Lin, A. Patel, and H. Y. Pu, Black hole shadow with soft hair, arXiv:2202.13559.
[22] C. Sun, Y. Liu, W. L. Qian, and R. Yue, Shadows of magnetically charged rotating black holes surrounded by quintessence, Chin. Phys. C **46**, 065103 (2022).
[23] İ. Çimdiker, D. Demir, and A. Övgün, Black hole shadow in symmergent gravity, Phys. Dark Universe **34**, 100900 (2021).
[24] Z. Zhong, Z. Hu, H. Yan, M. Guo, and B. Chen, QED effects on Kerr black hole shadows immersed in uniform magnetic fields, Phys. Rev. D **104**, 104028 (2021).
[25] Y. Hou, M. Guo, and B. Chen, Revisiting the shadow of braneworld black holes, Phys. Rev. D **104**, 024001 (2021).
[26] X. C. Cai and Y. G. Miao, Can we know about black hole thermodynamics through shadows?, arXiv:2107.08352.
[27] Q. Gan, P. Wang, H. Wu, and H. Yang, Photon spheres and spherical accretion image of a hairy black hole, Phys. Rev. D **104**, 024003 (2021).
[28] Z. Chang and Q. H. Zhu, The observer-dependent shadow of the Kerr black hole, J. Cosmol. Astropart. Phys. 09 (2021) 003.
[29] M. Wang, S. Chen, and J. Jing, Kerr black hole shadows in Melvin magnetic field with stable photon orbits, Phys. Rev. D **104**, 084021 (2021).
[30] R. Shaikh, S. Paul, P. Banerjee, and T. Sarkar, Shadows and thin accretion disk images of the γ-metric, arXiv:2105.12057.
[31] H. Guo, H. Liu, X. M. Kuang, and B. Wang, Acoustic black hole in Schwarzschild spacetime: Quasi-normal modes, analogous Hawking radiation and shadows, Phys. Rev. D **102**, 124019 (2020); Shadow and near-horizon characteristics of the acoustic charged black hole in curved spacetime, Phys. Rev. D **104**, 104003 (2021).

[32] K. Hioki and K. i. Maeda, Measurement of the Kerr spin parameter by observation of a compact object's shadow, Phys. Rev. D **80**, 024042 (2009).
[33] R. Kumar and S. G. Ghosh, Black hole parameter estimation from its shadow, Astrophys. J. **892**, 78 (2020).
[34] J. Bada and E. F. Eiroa, Shadow of axisymmetric, stationary, and asymptotically flat black holes in the presence of plasma, Phys. Rev. D **104**, 084055 (2021).
[35] S. W. Wei and Y. X. Liu, Observing the shadow of Einstein-Maxwell-Dilaton-Axion black hole, J. Cosmol. Astropart. Phys. 11 (2013) 063.
[36] A. Allahyari, M. Khodadi, S. Vagnozzi, and D. F. Mota, Magnetically charged black holes from non-linear electrodynamics and the event horizon telescope, J. Cosmol. Astropart. Phys. 02 (2020) 003.
[37] O. Y. Tsupko, Analytical calculation of black hole spin using deformation of the shadow, Phys. Rev. D **95**, 104058 (2017).
[38] P. V. P. Cunha, C. A. R. Herdeiro, and E. Radu, Spontaneously Scalarized Kerr Black Holes in Extended Scalar-Tensor–Gauss-Bonnet Gravity, Phys. Rev. Lett. **123**, 011101 (2019).
[39] R. Kumar and S. G. Ghosh, Rotating black holes in 4*D* Einstein-Gauss-Bonnet gravity and its shadow, J. Cosmol. Astropart. Phys. 07 (2020) 053.
[40] C. Y. Chen, Rotating black holes without $\mathbb{Z}_2$ symmetry and their shadow images, J. Cosmol. Astropart. Phys. 05 (2020) 040.
[41] S. Brahma, C. Y. Chen, and D. h. Yeom, Testing Loop Quantum Gravity from Observational Consequences of Nonsingular Rotating Black Holes, Phys. Rev. Lett. **126**, 181301 (2021).
[42] A. Belhaj, M. Benali, A. E. Balali, W. E. Hadri, and H. El Moumni, Shadows of charged and rotating black holes with a cosmological constant, Int. J. Geom. Methods Mod. Phys. **18**, 2150188 (2021).
[43] B. H. Lee, W. Lee, and Y. S. Myung, Shadow cast by a rotating black hole with anisotropic matter, Phys. Rev. D **103**, 064026 (2021).
[44] J. Badía and E. F. Eiroa, Influence of an anisotropic matter field on the shadow of a rotating black hole, Phys. Rev. D **102**, 024066 (2020).
[45] E. Frion, L. Giani, and T. Miranda, Black hole shadow drift and photon ring frequency drift, arXiv:2107.13536.
[46] R. Roy, S. Vagnozzi, and L. Visinelli, Superradiance evolution of black hole shadows revisited, Phys. Rev. D **105**, 083002 (2022).
[47] M. Afrin, R. Kumar, and S. G. Ghosh, Parameter estimation of hairy Kerr black holes from its shadow and constraints from M87*, Mon. Not. R. Astron. Soc. **504**, 5927 (2021).
[48] R. Kumar, S. G. Ghosh, and A. Wang, Shadow cast and deflection of light by charged rotating regular black holes, Phys. Rev. D **100**, 124024 (2019).
[49] S. K. Jha and A. Rahaman, Study of shadow and parameter estimation of non-commutative Kerr-like Lorentz violating black holes, arXiv:2111.02817.
[50] S. G. Ghosh, R. Kumar, and S. U. Islam, Parameters estimation and strong gravitational lensing of nonsingular Kerr-Sen black holes, J. Cosmol. Astropart. Phys. 03 (2021) 056.
[51] C. Bambi, K. Freese, S. Vagnozzi, and L. Visinelli, Testing the rotational nature of the supermassive object M87* from the circularity and size of its first image, Phys. Rev. D **100**, 044057 (2019).
[52] M. Khodadi, G. Lambiase, and D. F. Mota, No-hair theorem in the wake of event horizon telescope, J. Cosmol. Astropart. Phys. 09 (2021) 028.
[53] M. Afrin and S. G. Ghosh, Constraining rotating black holes in Horndeski theory with EHT observations of M87*, Astrophys. J. **932**, 51 (2022).
[54] P. V. P. Cunha and C. A. R. Herdeiro, Shadows and strong gravitational lensing: A brief review, Gen. Relativ. Gravit. **50**, 42 (2018).
[55] V. Perlick and O. Y. Tsupko, Calculating black hole shadows: Review of analytical studies, Phys. Rep. **947**, 1 (2022).
[56] K. Akiyama *et al.* (Event Horizon Telescope Collaboration), First M87 event horizon telescope results. I. The shadow of the supermassive black hole, Astrophys. J. Lett. **875**, L1 (2019).
[57] K. Akiyama *et al.* (Event Horizon Telescope Collaboration), First M87 event horizon telescope results. IV. Imaging the central supermassive black hole, Astrophys. J. Lett. **875**, L4 (2019).
[58] K. Akiyama *et al.* (Event Horizon Telescope Collaboration), First M87 event horizon telescope results. V. Physical origin of the asymmetric ring, Astrophys. J. Lett. **875**, L5 (2019).
[59] P. Kocherlakota *et al.* (Event Horizon Telescope Collaboration), Constraints on black-hole charges with the 2017 EHT observations of M87*, Phys. Rev. D **103**, 104047 (2021).
[60] P. V. P. Cunha, C. A. R. Herdeiro, and E. Radu, EHT constraint on the ultralight scalar hair of the M87 supermassive black hole, Universe **5**, 220 (2019).
[61] M. Khodadi, A. Allahyari, S. Vagnozzi, and D. F. Mota, Black holes with scalar hair in light of the event horizon telescope, J. Cosmol. Astropart. Phys. 09 (2020) 026.
[62] M. Fathi, M. Olivares, and J. R. Villanueva, Ergosphere, photon region structure, and the shadow of a rotating charged Weyl black hole, Galaxies **9**, 43 (2021).
[63] H. S. Liu and H. Lu, Charged rotating ads black hole and its thermodynamics in conformal gravity, J. High Energy Phys. 02 (2013) 139.
[64] H. Weyl, Reine infinitesimalgeometrie, Math. Z. **2**, 384 (1918).
[65] P. D. Mannheim and D. Kazanas, Exact vacuum solution to conformal Weyl gravity and galactic rotation curves, Astrophys. J. **342**, 635 (1989).
[66] G. U. Varieschi, A kinematical approach to conformal cosmology, Gen. Relativ. Gravit. **42**, 929 (2010).
[67] G. 't Hooft, Probing the small distance structure of canonical quantum gravity using the conformal group, arXiv:1009.0669.
[68] G. 't Hooft, Local conformal symmetry: The missing symmetry component for space and time, arXiv:1410.6675.
[69] C. M. Bender and P. D. Mannheim, No-ghost theorem for the fourth-order derivative Pais-Uhlenbeck oscillator model, Phys. Rev. Lett. **100**, 110402 (2008).
[70] P. D. Mannheim and A. Davidson, Fourth order theories without ghosts, arXiv:hep-th/0001115.
[71] P. D. Mannheim, Making the case for conformal gravity, Found. Phys. **42**, 388 (2012).

[72] J. Maldacena, Einstein gravity from conformal gravity, arXiv:1105.5632.
[73] J. R. Mureika and G. U. Varieschi, Black hole shadows in fourth-order conformal Weyl gravity, Can. J. Phys. **95**, 1299 (2017).
[74] B. Carter, Global structure of the Kerr family of gravitational fields, Phys. Rev. **174**, 1559 (1968).
[75] A. Grenzebach, V. Perlick, and C. Lämmerzahl, Photon regions and shadows of Kerr-Newman-NUT black holes with a cosmological constant, Phys. Rev. D **89**, 124004 (2014).
[76] N. Tsukamoto, Black hole shadow in an asymptotically-flat, stationary, and axisymmetric spacetime: The Kerr-Newman and rotating regular black holes, Phys. Rev. D **97**, 064021 (2018).
[77] S. V. M. C. B. Xavier, P. Cunha, V. P., L. C. B. Crispino, and C. A. R. Herdeiro, Shadows of charged rotating black holes: Kerr–Newman versus Kerr–Sen, Int. J. Mod. Phys. D **29**, 2041005 (2020).
[78] C. T. Cunningham and J. M. Bardeen, The optical appearance of a star orbiting an extreme Kerr black hole, Astrophys. J. Lett. Ed. **173**, L137 (1972).
[79] S. G. Ghosh, M. Amir, and S. D. Maharaj, Ergosphere and shadow of a rotating regular black hole, Nucl. Phys. **B957**, 115088 (2020).
[80] R. Craig Walker, P. E. Hardee, F. B. Davies, C. Ly, and W. Junor, The structure and dynamics of the subparsec jet in M87 based on 50 VLBA observations over 17 Years at 43 GHz, Astrophys. J. **855**, 128 (2018).
[81] V. Perlick, Gravitational lensing from a spacetime perspective, Living Rev. Relativity **7**, 9 (2004).
[82] W. Hasse and V. Perlick, A morse-theoretical analysis of gravitational lensing by a Kerr-Newman black hole, J. Math. Phys. (N.Y.) **47**, 042503 (2006).